Deformation of The Human Brain Induced By Mild Angular Head Acceleration

Arash A. Sabet[1], **Eftychios Christoforou**[3], **Benjamin Zatlin**[4], **Guy M. Genin**[1], and **Philip V. Bayly**[1,2]

[1]*Department of Mechanical, Aerospace and Structural Engineering, Washington University, St. Louis, Missouri, USA*

[2]*Department of Biomedical Engineering, Washington University, St. Louis, Missouri, USA*

[3]*Department of Electrical and Computer Engineering, University of Cyprus, Nicosia, Cyprus*

[4]*Biomedical Engineering, University of Southern California, Los Angeles, California, USA*

Abstract

Deformation of the human brain was measured in tagged magnetic resonance images (MRI) obtained dynamically during angular acceleration of the head. This study was undertaken to provide quantitative experimental data to illuminate the mechanics of traumatic brain injury (TBI). Mild angular acceleration was imparted to the skull of a human volunteer inside an MR scanner, using a custom MR-compatible device to constrain motion. A grid of MR "tag" lines was applied to the MR images via spatial modulation of magnetization (SPAMM) in a fast gradient echo imaging sequence. Images of the moving brain were obtained dynamically by synchronizing the imaging process with the motion of the head. Deformation of the brain was characterized quantitatively via Lagrangian strain. Consistent patterns of radial-circumferential shear strain occur in the brain, similar to those observed in models of a viscoelastic gel cylinder subjected to angular acceleration. Strain fields in the brain, however, are clearly mediated by the effects of heterogeneity, divisions between regions of the brain (such as the central fissure and central sulcus) and the brain's tethering and suspension system, including the dura mater, falx cerebri and tentorium membranes.

1. Introduction

Every year there are over 1.5 million new cases of TBI in the US. In addition to the devastating human costs, TBI causes over $56.3 billion in economic losses per year (Thurman, 2001). In spite of its importance and its many years of research interest, TBI is not well understood. It is clear that when the skull is accelerated, the brain deforms in response, but the details of the resulting strain fields are not known. It is widely accepted that skull acceleration can lead to brain injury if local strains and strain rates exceed a critical threshold (Gennarelli et al., 2001; Bain and Meaney, 2000), above which the neural fibers (axons) are affected.

Shear strains due to angular acceleration of the skull have been hypothesized to be especially important in TBI. Holbourn (1943) showed that rotation of the human skull could cause large

deformations of a gel housed within its cranial cavity. Pudenz and Shelden (1946) supported Holbourn's claims through visualization of the surface of animal brains. They replaced the top half of a monkey skull with transparent plastic, and filmed the deformation of the brain during linear acceleration.

More recently, quantitative studies of brain deformation have been performed using high-speed filming of gel-filled skulls (Meaney et al., 1995; Margulies et al., 1990), high-speed bi-planar x-ray imaging of the cadaveric brain (Hardy et al., 2001) and MR imaging of the brain in human volunteers (Wedeen and Poncelet, 1996; Reese et al., 2002; Bayly et al., 2005). In studies done with high-speed filming, quantitative estimates of strain (0.20-0.30) were found in gel-filled pig skulls subjected to angular accelerations similar to those that produced axonal injury in the live animal. Because these studies used gel as a surrogate, they could not capture the effects of heterogeneity, anisotropy, vasculature, meninges, and cerebrospinal fluid on brain deformation. Hardy et al. (2001) performed high-speed (250-1000 frames/second) bi-planar x-ray studies of the displacement of eleven neutrally buoyant radio-opaque markers in cadaver brains during head acceleration. Spatial resolution was limited by the sparseness of the array of physical markers; also tissue properties and brain-skull interactions of the cadaver may differ significantly from those of a live subject. Zou et al. (2007) reported estimates of relative rigid-body rotation and translation of the brain and skull, obtained from the x-ray data of Hardy et al. (2001). Wedeen and Poncelet (1996) demonstrated the use of phase-contrast MRI to measure strains in the brain parenchyma of human subjects during physiological pulsatile motion and voluntary head shaking. Head accelerations during voluntary motion were not measured. Bayly and co-workers (2005) studied deformation of the human brain *in vivo*, during controlled linear head acceleration, using tagged MR imaging. This approach provides strain fields with good spatial (2×2×5 mm) and temporal (6 ms/frame) resolution. Results of this study suggest that tethering of the brain at the sellar and suprasellar region plays a central role in determining the mechanical response of the brain during linear skull accelerations (Bayly et al., 2005). Head accelerations were primarily posterior-anterior and were limited to values that are safe for the human test subjects (20-30 m/sec^2).

An important purpose for measurement of brain deformation is to generate quantitative data to validate computer models. Computer models of the brain (Ruan et al, 1991; Kleiven, 2006; Takhounts et al., 2003; Zhang et al., 2004) offer great potential for studying brain biomechanics, if they are shown to be accurate. For example, simulations could be used to provide estimates of brain deformation for accelerations that would be unsafe for human subjects (as in, for example, Kleiven and von Holst, 2002), or for studies that would be costly, difficult, or inconclusive with cadavers or animals. However, accurate computer simulations require accurate information about the brain's material properties, boundary conditions, and tissue connectivity. It is critically important for computer simulations to be verified by comparison to observations.

The current experimental study was performed to illuminate the mechanical response of the brain to mild *angular* acceleration. The brain was imaged using dynamic tagged, gated MRI during angular motion of the head in the transverse plane (rotation about the long axis of the neck). Deformation was quantified by computing the two-dimensional (2-d) Lagrangian strain tensor in four parallel axial planes.

2. Methods

2.1 Overview

Three adult male subjects of average height and weight (age 25-42 yrs; 70-80 kg; 1.7 – 1.8 m tall), performed controlled head rotation using a custom, MR-compatible device (Figure 1) that imparted a repeatable mild angular acceleration of ~250-300 rad/s^2. These accelerations are

about 10% of those experienced during heading of a soccer ball (Naunheim et al., 2003). The protocol was reviewed and approved by the Washington University Human Research Protection Office. Tagged MR images were acquired in 3-4 axial planes in each subject. Images of different planes in the same subject were acquired on different days.

2.2 Head Rotation

A custom MR-compatible head rotator (built in the Washington University Instrument Shop) was used to impart mild angular accelerations to the head of a test subject (Figure 1). The head cylinder, which cradles the subject's head, was designed to fit inside the head coil of a Siemens Sonata MRI (Siemens, Munich, Germany) and rotate freely about a plastic bearing at the back of the device. Rotation was initiated by releasing a latch, which allowed the plastic counterweight to apply torque to the head cylinder Release of the latch also tripped a fiber optic switch that activated a TTL pulse to the MRI, initiating the scanning sequence. After approximately 200 ms, the weight impacted a stop pin, imparting an impulse to the rotating assembly (Figure 1). The associated angular deceleration produced measurable deformation in the subject's brain.

The magnitudes of angular acceleration experienced by each subject were found by recording the linear tangent acceleration at a site on the head cylinder 10 cm from the axis of rotation. A representative time series of angular acceleration from subject S2 is shown in Figure 2. The duration of the peak acceleration pulse was approximately 40 ms. The magnitude of angular acceleration for subject S1 was 299 ± 29 rad/s^2; for subject S2, it was 244 ± 7 rad/s^2; and for subject S3, 370 ± 21 rad/s^2 (mean $\pm$ std. deviation). These values are roughly 10-15% of those experienced by soccer players during voluntary impact between the head and soccer ball (Naunheim et al., 2003).

2.3 Imaging Protocol

The FLASH2D MR cine sequence was used to collect tagged images of the deformed brain. The sequence had a frame rate of 6 ms and an echo time TE= 2.9 ms. For each nominally identical repetition of the head rotation, a single line of k-space data (192 samples) was collected 90 times; each acquisition separated by 6 ms. The phase encoding-gradient was incremented after each repetition of motion. In total, 144 rotations of the head were required, leading to a 192×144 data matrix (image) for each of the 90 time points.

To superimpose tag lines on the image, immediately after the latch was released, radio-frequency (RF) pulses were applied in combination with magnetic gradients. This sequence causes longitudinal magnetization of spins to vary spatially in a sinusoidal fashion (Axel and Dougherty, 1989), resulting in an image superimposed with an array of light and dark lines. These "tag lines" move with the tissue, and their intersections may be tracked to characterize motion.

Images were collected in axial planes at several levels (Figure 3). The reference plane (0 cm height) passed through the genu and splenium of the corpus callosum. Images were also acquired from parallel planes 2 cm and 4 cm superior to the reference plane, denoted as +2 cm and +4 cm, and 1 cm inferior (-1 cm).

2.4 Strain Estimation Procedures

The analysis of deformation is illustrated in Figure 4. Tag-line intersections were identified and tracked using contours of "harmonic phase" (HARP) (Figures 4b and 4f), via the method developed by Osman et al. (2000). Intersection points in reference (pre-impact) and deformed (post-impact) configurations were registered to one another, and used to generate a common

mesh of triangular elements (Figures 4c and 4g). The deformation gradient tensor, $\mathbf{F}$, was obtained by fitting the equation:

$$d\mathbf{x}_i = \mathbf{F} d\mathbf{X}_i \quad i = 1, 2, 3,$$

(1)

where $d\mathbf{X}_i$ is a vector from one triangle vertex to another in the reference configuration, and $d\mathbf{x}_i$ is that same segment in the deformed configuration (Figure 5). A custom algorithm written in MATLAB (Mathworks, Natick, MA) (Bayly et al., 2005) was used to solve for the deformation gradient tensor, $\mathbf{F}$.

Once $\mathbf{F}$ was determined from the reference and deformed tagged images, the Lagrangian strain tensor, $\mathbf{E}$, was calculated in the Cartesian image coordinate system:

$$\mathbf{E} = \frac{1}{2} \left(\mathbf{F}^T \mathbf{F} - \mathbf{I} \right).$$

(2)

Here $\mathbf{I}$ is the 2nd rank unit tensor, and $\mathbf{F}^T$ denotes the transpose of the deformation gradient tensor. We studied the planar components [$\mathbf{E}$] of the strain tensor $\mathbf{E}$ in a cylindrical coordinate system with the positive rotation axis ("z-axis") in the superior direction:

$$[\mathbf{E}] = \left[\begin{array}{cc} \varepsilon_{rr} & \varepsilon_{r\theta} \\ \varepsilon_{\theta r} & \varepsilon_{\theta\theta} \end{array} \right]$$

(3)

For angular acceleration of the skull, the dominant strain component is radial-circumferential shear, $\varepsilon_{r\theta}$.

3. Results

Patterns of deformation are illustrated qualitatively by the reference and deformed grids of tag lines in Figures 6 and 7. In these figures displacements are amplified by a factor of five, for visualization only. Figure 6 illustrates the initial deformation as mobile brain tissue rotates clockwise relative to the skull, which has stopped. Because the brain is tethered to the skull by vessels and membraneous connections (e.g., arachnoid granulations) at its base and surface, the decelerating torque is transmitted to the brain. Deformation is dominated by radial-circumferential shear; Figure 7 captures an opposite pattern of shear deformation as the brain nearly reverses this change of shape during viscoelastic oscillations.

These changes in shape may be quantified by strain. Sequences of strain fields in one subject (S1), at four image plane heights, over a time interval of 60 ms immediately after impact are shown in Figure 8. The heights of image planes are described relative to a reference transverse plane (0 cm) which passes approximately through the genu ("knee") and splenium of the corpus callosum. The component shown is the radial-circumferential shear strain: $\varepsilon_{r\theta}$.

Several consistent features are observed in the four different planes shown in Figure 8. Shear strain values peak approximately 30-60 ms after initial impact (impact was observed to begin at $t \approx 200$ ms), and then decay. Areas of high shear strain are approximately symmetric about two axes roughly aligned with the medial longitudinal fissure and the central sulcus. The largest positive shear strains at the +4 cm level seem to occur later than the largest strains at lower

levels (0 cm or +2 cm). This suggests that some torsional deformation may occur as material in the lower planes rotates relative to material in the upper plane. (Note, however, that the strain fields were obtained during different trials. Because the exact time of impact may vary between trials, the temporal relationship between strains at different levels can not be determined precisely.)

Figures 9, 10 and 11 show results from different subjects juxtaposed. Strain fields in subjects S1 and S2 at the +2 cm level are quite similar (Figure 9); both display the symmetries noted above with respect to the medial longitudinal fissure and central sulcus. Figure 10 shows strain fields from subjects S1 and S3 at the reference (0 cm) level; these fields are qualitatively similar to those in Figure 9. Figure 11 shows analogous results from subjects S1 and S3 at the +4 cm level. Although subject S3 exhibits somewhat smaller strains at this level (likely due to anatomical differences), both sequences of strain fields illustrate the later development of strain at the +4 cm level (Figure 11) compared to the +2 cm or 0 cm levels (Figures 9 and 10).

Temporal behavior may be characterized by depicting how much of the brain experiences a specific strain level at a given time. This is a measure that is medically relevant, because in more severe impacts high strain is likely to correspond to injury, and statistically robust. Figure 12 displays the fraction of the image plane in which radial-circumferential strain exceeds a specified level ε (for $\varepsilon=0.02$, $\varepsilon=0.04$, $\varepsilon=0.06$). The frames of Figure 12 correspond to the sequences of images in Figures 9. This representation illustrates the prevalence of small strains (at this level almost 70% of the brain experiences strain > 0.02) but the relative rarity of strains greater than 0.06. Baseline strain estimates before impact (not shown) are very small; strain has dissipated to low levels by 60 ms after impact.

The motion of the brain also includes a small rigid-body rotation relative to the skull. Although the tagging methods used in this study were not optimized to detect skull motion, it was possible to observe tangential displacements of approximately 2-3 mm between initially-adjacent points on the brain and skull. The rigid-body rotation of the brain was also estimated from the relative angle change between the anterior-posterior (long) axis of the skull and the corresponding long axis of the brain; relative rotation of 1°-2° was typical.

4. Discussion

The theory that radial-circumferential shear strain dominates during angular acceleration was first proposed by Holbourn (1943). Holbourn used a gelatin phantom inside a simulated skull to examine strain fields. Results from the present study support his basic theory, though strain patterns differ because Holbourn's simple models lacked true material properties and boundary conditions.

In the current study, values of radial-circumferential shear strain exceeding 0.06 were observed in small sections of several axial imaging planes, in response to angular head accelerations of approximately 250-300 rad/s^2. Large portions of these axial planes experienced strains greater than 0.02. Radial-circumferential shear strain fields are grossly similar to those that occur in a simple model: a brain-sized cylinder of homogeneous, viscoelastic gel (instantaneous shear modulus $G_0 = 1710$ Pa; long term shear modulus $G_\infty = 1334$ Pa; time constant $\tau=1.3$ ms) encased in a rigid shell undergoing and angular acceleration pulse of 250 rad/s^2 (Figure 13). Images of gel deformation were obtained using an analytical model and solution described in Bayly et al. (2007). The gel is intended only as a qualitative analog to the brain, but the shear moduli are within the range of values reported for fresh mammalian brain (e.g., Thibault and Margulies, 1998). Similarities between the brain and the gel model include the patterns of curvature in the "tag" lines due to shear deformation, the order of magnitude of strains, and the waxing and waning of shear strain levels due to viscoelastic oscillations. Differences

between the response of the brain and the gel cylinder are due to the effects of geometry, the complexity of the skull-brain interface, and the heterogeneity and anisotropy of brain tissue.

At +2 cm above the reference plane, all subjects experienced maximal deformation approximately 30 ms after impact, suggesting that their brain tissue viscoelastic time constants were similar. At the +4 cm level, strain magnitudes were typically lower, and apparently delayed relative to deformation at the +2 cm level. The membranes and vessels that tether the brain to the skull at its base and boundaries induce stress and strain at these sites. Measured strain fields also indicated an important role of a central dividing feature such as the falx. This is suggested by the patterns of symmetry and anti-symmetry observed in the $\varepsilon_{r\theta}$ shear strain fields. The medial longitudinal fissure appears to isolate the hemispheres of the brain in regions superior to the corpus callosum (the upper imaging planes). Furthermore, there seems to be decreased strain along the central sulcus, suggesting that the brain may also have mechanically isolated regions in the anterior-posterior direction. The specific roles of material heterogeneity, mechanical anisotropy, and boundary conditions remain topics of great interest. These roles will be explored in future work by continued imaging studies, and integration of these experimental data with computer simulations.

Small rigid-body rotations of the brain relative to the skull were observed as the skull decelerated. The anterior-posterior axis of the brain rotated 1°-2° relative to the analogous axis of the skull, and tangential displacements of 2-3 mm were observed between initially-adjacent points on the brain and skull. For comparison, studies by Ji et al. (2004; 2007) of quasi-static neck flexion (~50°) in the sagittal plane showed relative displacements of 1-3 mm between the brainstem and skull near the foramen magnum, and 2°-6° rotation of the cerebellum relative to the skull. An important difference between this study and those of Ji et al. is that in the current study inertial effects are responsible for relative rotation, whereas in the studies of quasi-static neck flexion, relative motion was produced by gravity and by tension in the spinal cord. Zou et al. (2007) describe brain motion induced by combined linear and angular acceleration of a cadaver head in the sagittal plane. In contrast, the present study involves almost pure angular acceleration of the living head in a transverse plane. The angular accelerations of the head reported by Zou et al. (2007) were higher than those in the current study (~1000-3000 rad/s^2 vs. 250-300 rad/s^2); the ensuing relative rigid-body rotation was also higher, but not proportionally so (5° vs. 1-2°). In the current study, no perceptible rigid-body translation of the brain was observed, although as noted, the methods were not optimized to detect minute translations. The amplitudes of relative brain-skull displacement that can be attributed to deformation and rigid-body rotation are similar: on the order of a few millimeters.

The spatial resolution of the MR images was limited by the constraints of the imaging process. Since one repetition of motion was required for each line of k-space, increasing the spatial resolution in the phase-encode direction would require increasing the number of repetitions the subject must perform. The resolution of the tagging pattern (spacing of tag lines) represents a compromise between increased spatial resolution and amplification of displacement errors (an effect of numerical differentiation) in the calculation of strain. The grid size in this study was based on experience gained from previous studies (Bayly et al., 2005). Increased "signal-to-noise" in strain estimates could be obtained by increasing the deformation in the samples. In this study, the gravitational force on a 600 g offset mass was used to drive the angular acceleration. This mass could be increased to deliver a larger force, producing a larger acceleration, and ultimately causing a larger deformation of the brain. This acceleration, however, could only be increased to a level deemed safe for the test subjects.

Temporal resolution of the MR cine sequence was determined by the time required to complete the steps in the MR pulse sequence, including data acquisition. A time step of 6 ms/per frame was attained in the current study. Using the existing gradient echo pulse sequence, slightly

better temporal resolution could be obtained by sacrificing spatial resolution in the read-out direction. Another way to increase the effective temporal resolution of the system would be to increase the duration of the deceleration (for example, by increasing the compliance of the stop pin). This approach would lead to smaller accelerations and reduced deformation.

The current study focuses on angular acceleration of the head in the tranverse plane. This motion is not intended to model a specific injury event, which would typically involve a combination of linear and angular accelerations. Rather, it provides a simplified case: almost pure rotation of the head about an axis that passes roughly through the middle of the brain, perpendicular to the imaging plane. One benefit is that ensuing deformations occur predominantly in the plane of rotation, and are thus well suited to 2-D analysis.

This study has provided new data on the deformation of the brain that occurs due to angular acceleration of the skull. This data should be immediately applicable to the validation of computer models of brain biomechanics. Although these experiments involve only relatively small deformations, they illustrate important qualitative features of the brain's response, which should be captured by any numerical simulation. Future work will include testing more human subjects, and will involve more imaging planes and types of motion. Future work should also involve studies with animals or post-mortem human subjects to obtain data during higher accelerations and larger deformations. Such studies could also provide more complete information on the three-dimensional deformation of the brain and its dependence on skull geometry, boundary conditions, material properties, and acceleration parameters.

Acknowledgments

References

Axel L, Dougherty L. MR imaging of motion with spatial modulation of magnetization. Radiology 1989;171(3):841–845. [PubMed: 2717762]

Bain AC, Meaney DF. Tissue-level thresholds for axonal damage in an experimental model of central nervous system white matter injury. Journal of Biomechanical Engineering 2000;122:615–622. [PubMed: 11192383]

Bayly PV, Cohen TS, Leister EP, Ajo D, Leuthardt EC, Genin GM. Deformation of the human brain induced by mild acceleration. Journal of Neurotrauma 2005;22(8):845–56. [PubMed: 16083352]

Bayly PV, Massouros PG, Sabet AA, Genin GM. Magnetic resonance rheometry of transient shear wave propagation in a viscoelastic gel cylinder. 2007In review

Gennarelli TA, Thibault LE, Tipperman R, Tomei G, Sergot R, Brown M, Maxwell WL, Graham DI, Adams JH, Irvine A, et al. Axonal injury in the optic nerve: a model simulating diffuse axonal injury in the brain. Journal of Neurosurgery 1989;71(2):244–53. [PubMed: 2746348]

Hardy WN, Foster CD, Mason MJ, Yang KH, King AI, Tashman S. Investigation of head injury mechanisms using neutral density technology and high-speed biplanar X-ray. Stapp Car Crash Journal 2001;45:337–368. [PubMed: 17458753]

Holbourn AHS. The mechanics of head injuries. Lancet 1943;2:438–441.

Ji S, Zhu Q, Dougherty L, Margulies SS. In vivo measurements of human brain displacement. Stapp Car Crash Journal 2004;48:227–37. [PubMed: 17230268]

Ji S, Margulies SS. In vivo pons motion within the skull. Journal of Biomechanics 2007;40:92–99. [PubMed: 16387309]

Kleiven S, von Holst H. Consequences of head size following trauma to the human head. Journal of Biomechanics 2002;35:153–60. [PubMed: 11784533]

Kleiven S. Evaluation of head injury criteria using a finite element model validated against experiments on localized brain motion, intracerebral acceleration, and intracranial pressure. International Journal of Crashworthiness 2006;11:65–79.

Margulies SS, Thibault LE, Gennarelli TA. Physical model simulations of brain injury in the primate. Journal of Biomechanics 1990;23:832–836.

Meaney DF, Smith DH, Ross DT, Gennarelli TA. Biomechanical analysis of experimental diffuse axonal injury in the miniature pig. Journal of Neurotrauma 1995;12(4):689–695. [PubMed: 8683620]

Naunheim RS, Bayly PV, Standeven J, Neubauer JS, Lewis LM, Genin GM. Linear and angular accelerations during heading of a soccer ball. Medicine and Science in Sports and Exercise 2003;35 (8):1406–12. [PubMed: 12900697]

Osman NF, McVeigh ER, Prince JL. Imaging heart motion using harmonic phase MRI. IEEE Transactions on Medical Imaging 2000;19:186–202. [PubMed: 10875703]

Reese TG, Feinberg DA, Dou J, Wedeen VJ. Phase contrast MRI of myocardial 3D strain by encoding contiguous slices in a single shot. Magnetic Resonance in Medicine 2002;47:665–676. [PubMed: 11948727]

Ruan JS, Khalil T, King AI. Human head dynamic response to side impact by finite element modeling. Journal of Biomechanical Engineering 1991;113:276–283. [PubMed: 1921354]

Thibault KL, Margulies SS. Age-dependent material properties of the porcine cerebrum: Effect on pediatric inertial head injury criteria. Journal of Biomechanics 1998;31:1119–1126. [PubMed: 9882044]

Takhounts EG, Eppinger RH, Campbell JQ, Tannous RE, Power ED, Shook LS. On the development of the SIMon finite element head model. Stapp Car Crash Journal 2003;47:107–33. [PubMed: 17096247]

Thurman, D. The epidemiology and economics of head trauma. In: Miller, L.; Hayes, R., editors. Head Trauma: Basic, Preclinical, and Clinical Directions. John Wiley and Sons; New York: 2001.

Wedeen, V.; Poncelet, BP. MRI of brain parenchymal motion. In: Grant, DM.; Harris, RK., editors. Encyclopedia of Nuclear Magnetic Resonance. John Wiley and Sons; New York: 1996.

Zhang L, Yang KH, King AI. A proposed injury threshold for mild traumatic brain Injury. Journal of Biomechanical Engineering 2004;126:226–236. [PubMed: 15179853]

Zou H, Schmiedeler JP, Hardy WN. Separating brain motion into rigid body displacement and deformation under low-severity impacts. Journal of Biomechanics 2007;40:1183–1191. [PubMed: 16919640]
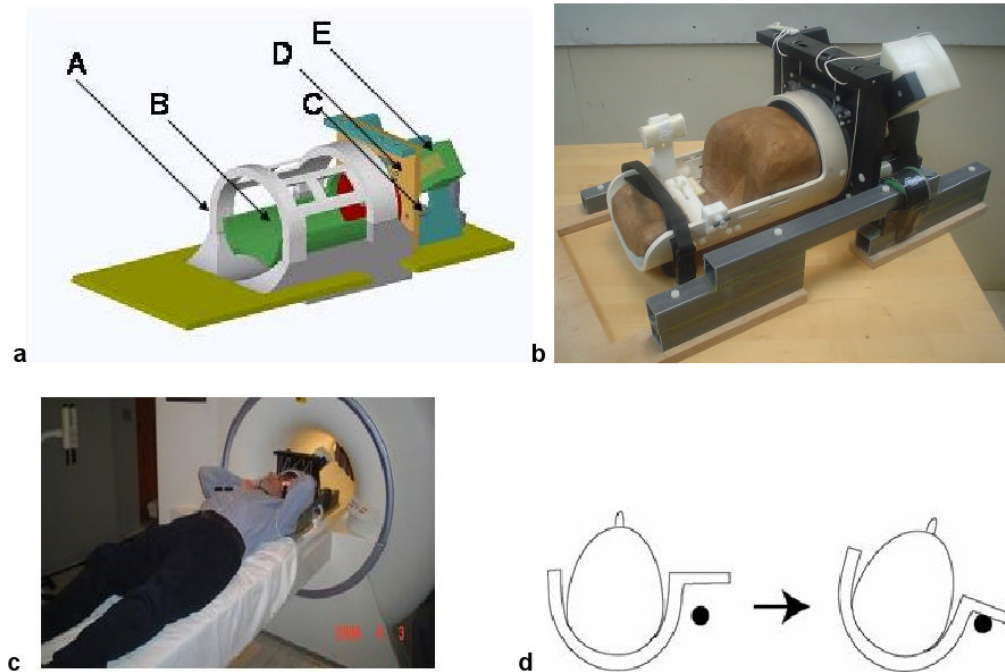
Figure 1.
(a) Digital solid model of the device used to constrain head rotation in the MR scanner. (A) The MR head coil (antenna). (B) The rotating head cylinder. (C) The pin used to stop angular rotation. (D) Latch, which is released to initiate motion. (E) Plastic counterweight (600 grams). (b) Photograph of the physical device. (c) The head of the subject was secured inside the head rotator, and the entire assembly translated into the MRI coil for imaging. (d) Upon release of a latch, the head was rotated by the off-axis weight until it was abruptly stopped by a compliant pin. This soft stop provided approximately 250-300 rad/s^2 angular deceleration.
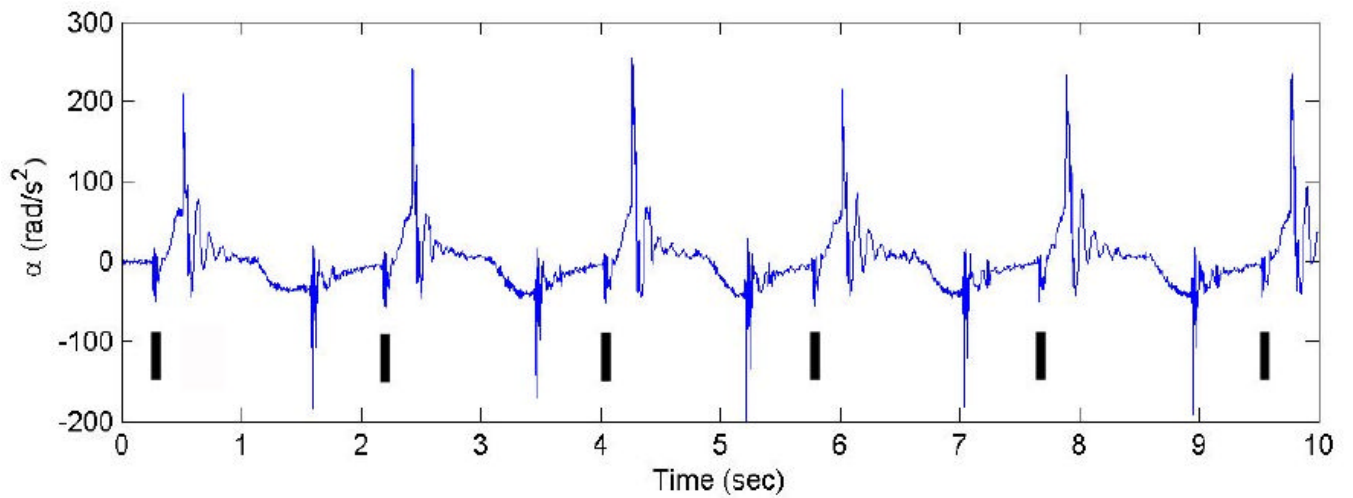
Figure 2.
Angular acceleration measurements recorded during repeated controlled head rotation (subject S2). Black bars indicate the volunteer-initiated latch release that initiated motion and triggered the scanning sequence; image data were acquired in the subsequent 540 ms.
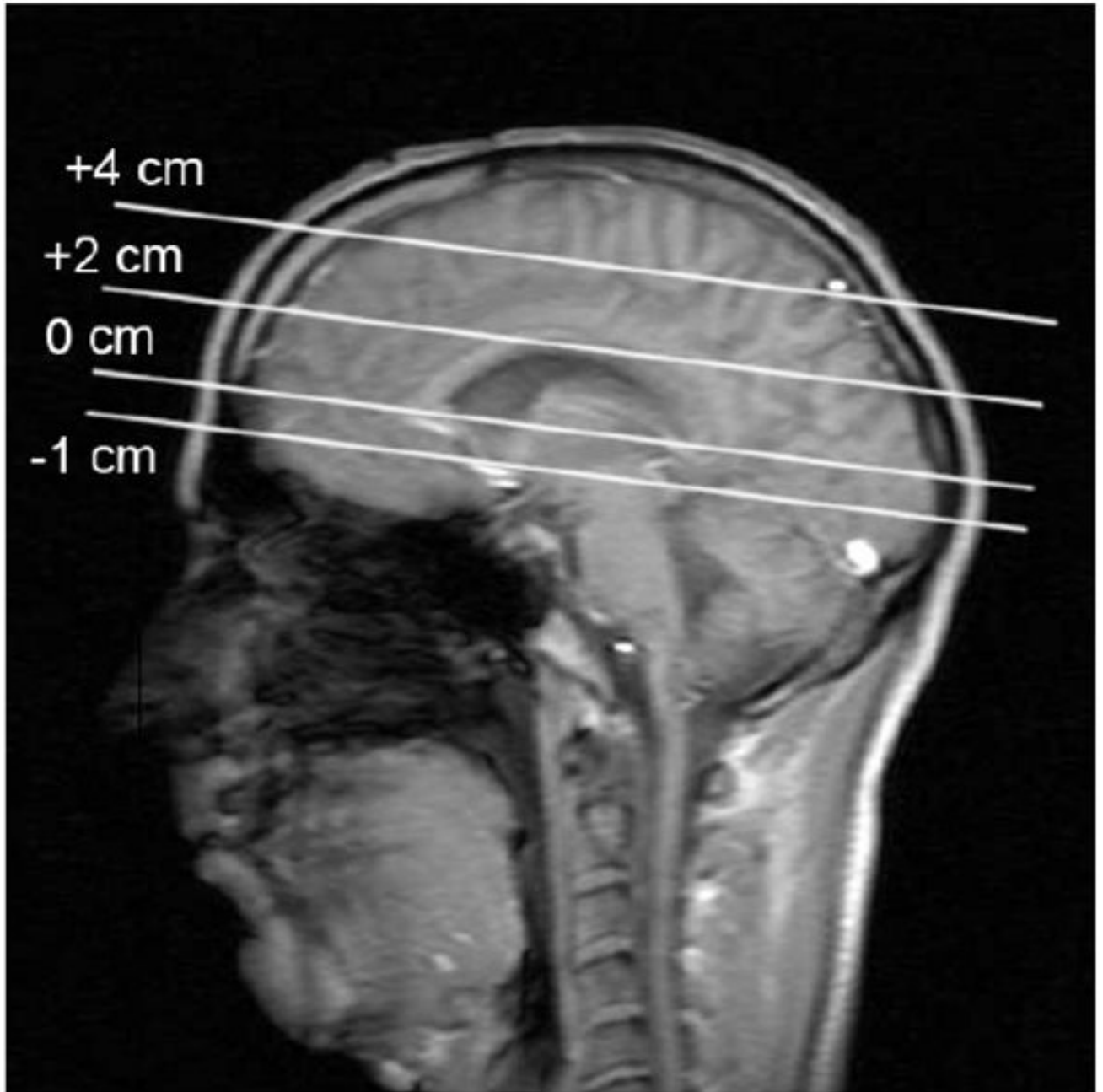
Figure 3.
Sagittal image illustrating the positions at which MR images were taken. The axial planes in which deformation data were collected are described with respect to a reference plane passing through the genu and splenium of the corpus callosum.
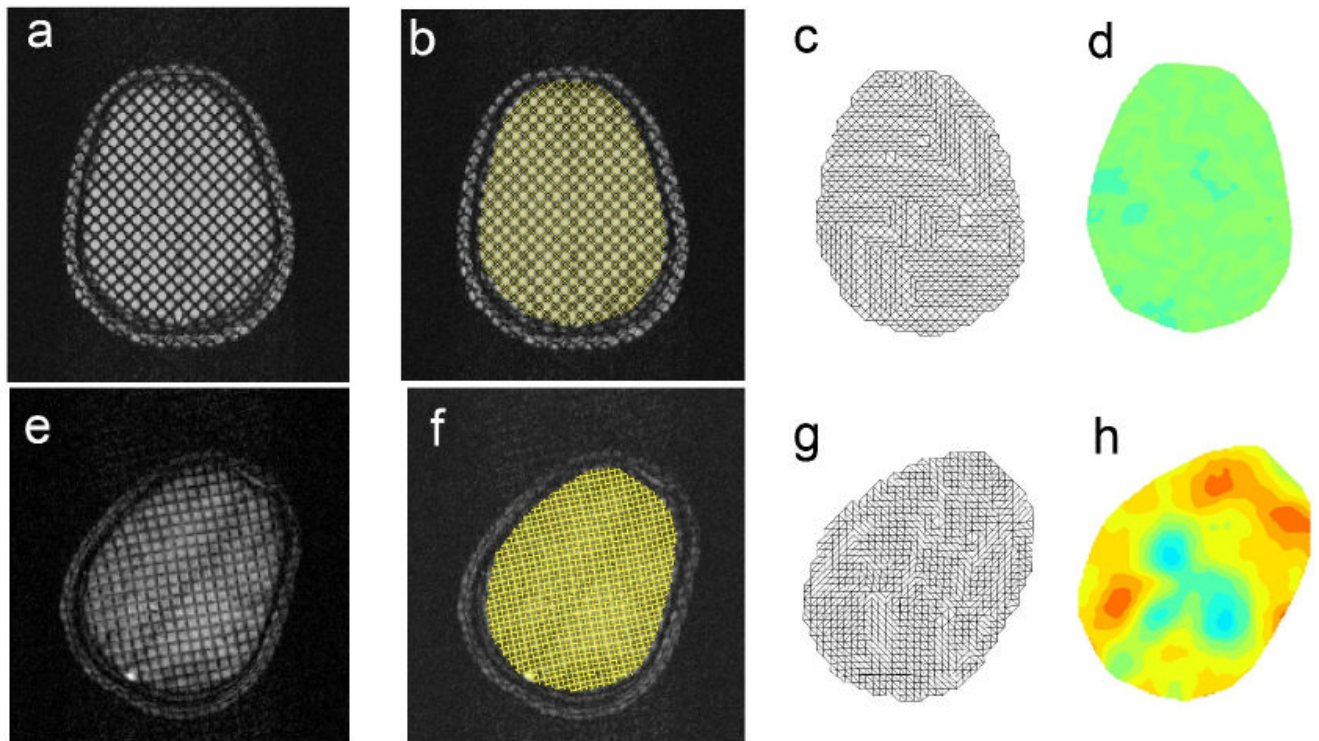
Figure 4.
Illustration of strain estimation procedures. Reference image (top, a-d) and deformed images (bottom, e-h). (a, e) Tagged images. (b, f) HARP contours (synthetic tag lines). (c, g) triangular meshes generated from intersection points of HARP contours. (d, h) Radial-circumferential shear strain ($\varepsilon_{r\theta}$) fields.
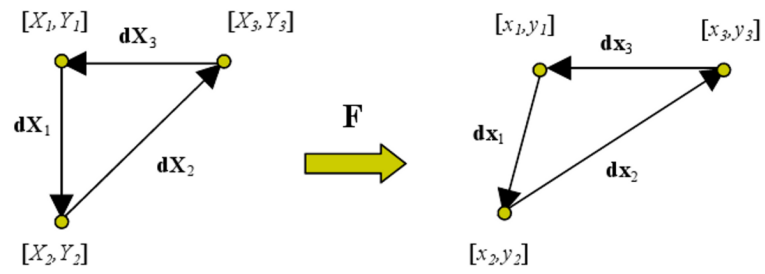
Figure 5.
The deformation gradient tensor, **F**, maps each side of the reference triangle into a corresponding side of the deformed triangle (Eq. 1).
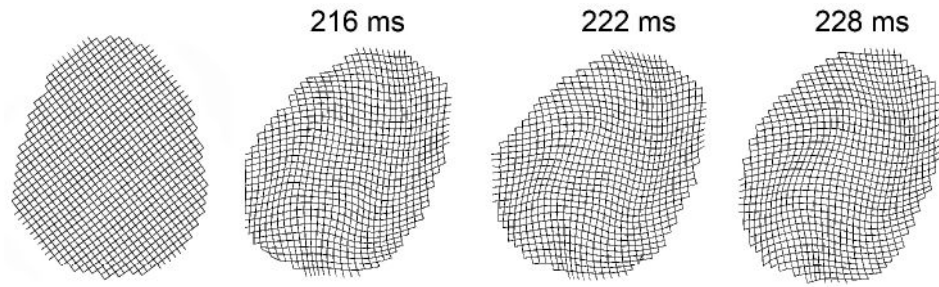
Figure 6.
Grids of tag lines (HARP contours) showing "clockwise" shear deformation of the brain relative to the skull in subject S1. Displacements are scaled by a factor of five for visualization.
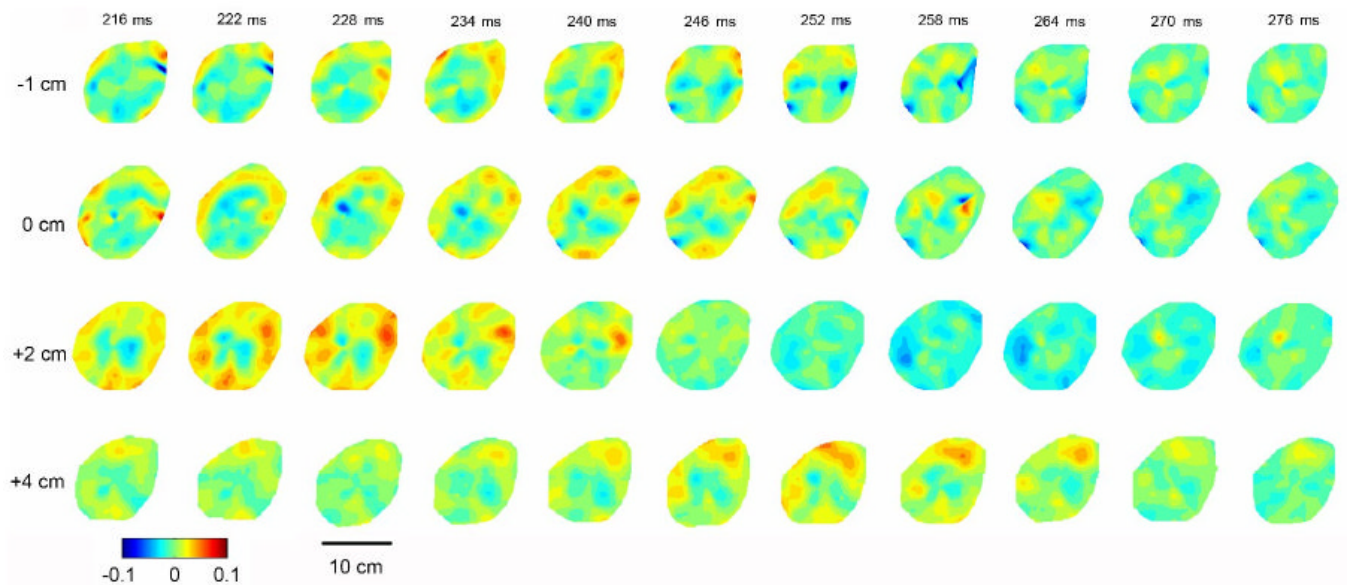
264 ms   270 ms   276 ms
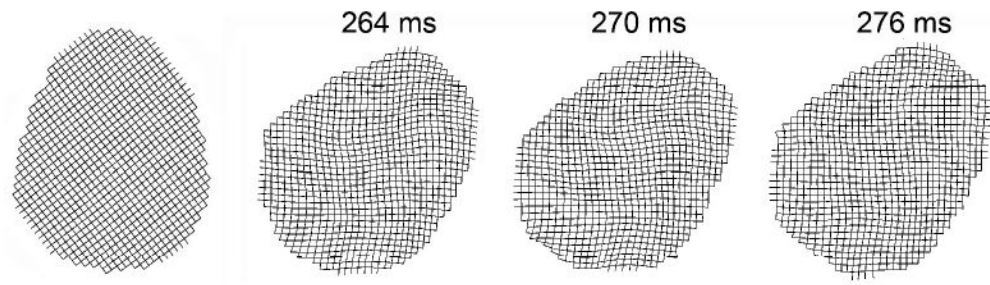
Figure 7.
Grids of tag lines (HARP contours) showing "counterclockwise" shear deformation of the brain as it undergoes viscoelastic oscillation in subject S1. Displacements are scaled by a factor of five for visualization.

Figure 8.
Radial-circumferential shear strain $\varepsilon_{r\theta}$ in subject S1 in four axial planes (-1 cm, 0 cm, +2 cm, +4 cm). Data are presented chronologically after initiation of the MR imaging sequence at the onset of head rotation (t=0 ms). Impact occurs at approximately t=200 ms.
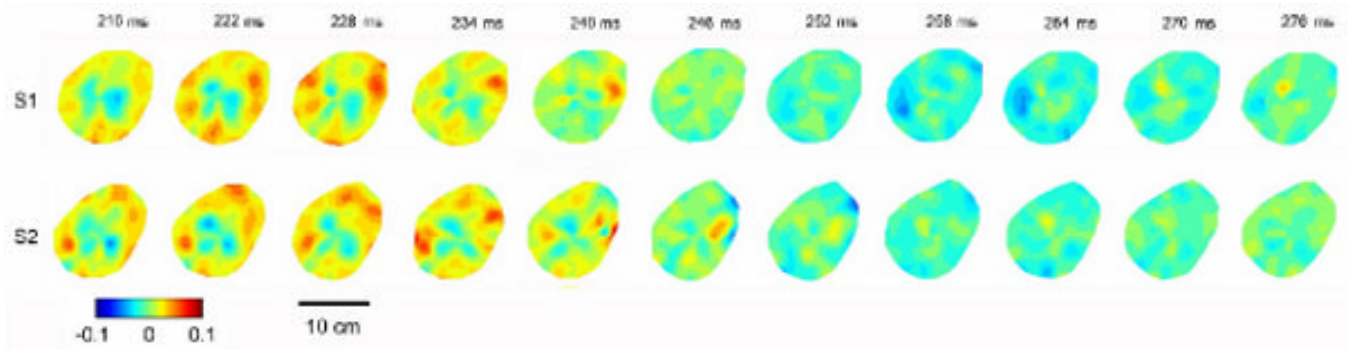
Figure 9.
Radial-circumferential shear strain $\varepsilon_{r\theta}$ in the axial plane +2 cm above the reference plane in two subjects (S1 and S2). Data are presented chronologically after initiation of the MR imaging sequence at the onset of head rotation (t=0ms).
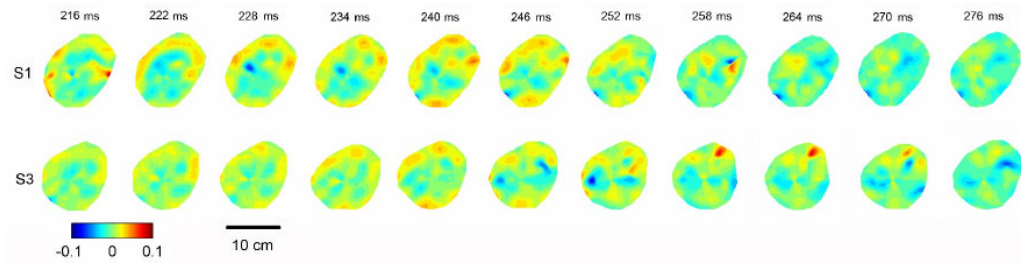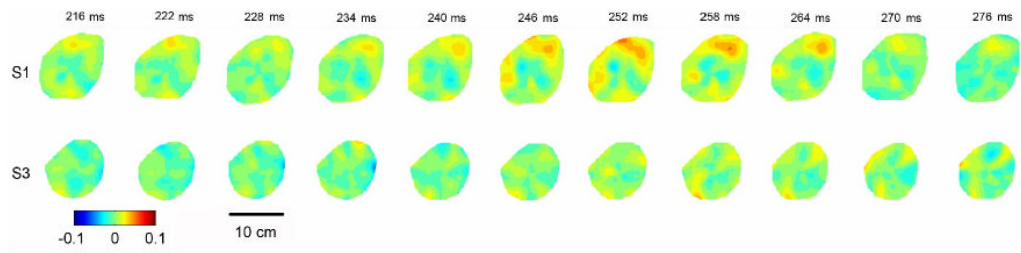
Figure 10.
Radial-circumferential shear strain $\varepsilon_{r\theta}$ in the axial reference plane (0 cm) in two subjects (S1 and S3). Data are presented chronologically after initiation of the MR imaging sequence at the onset of head rotation (t=0ms).

Figure 11.
Radial-circumferential shear strain $\varepsilon_{r\theta}$ in the axial plane +4 cm above the reference plane in two subjects (S1 and S3). Data are presented chronologically after initiation of the MR imaging sequence at the onset of head rotation (t=0ms).
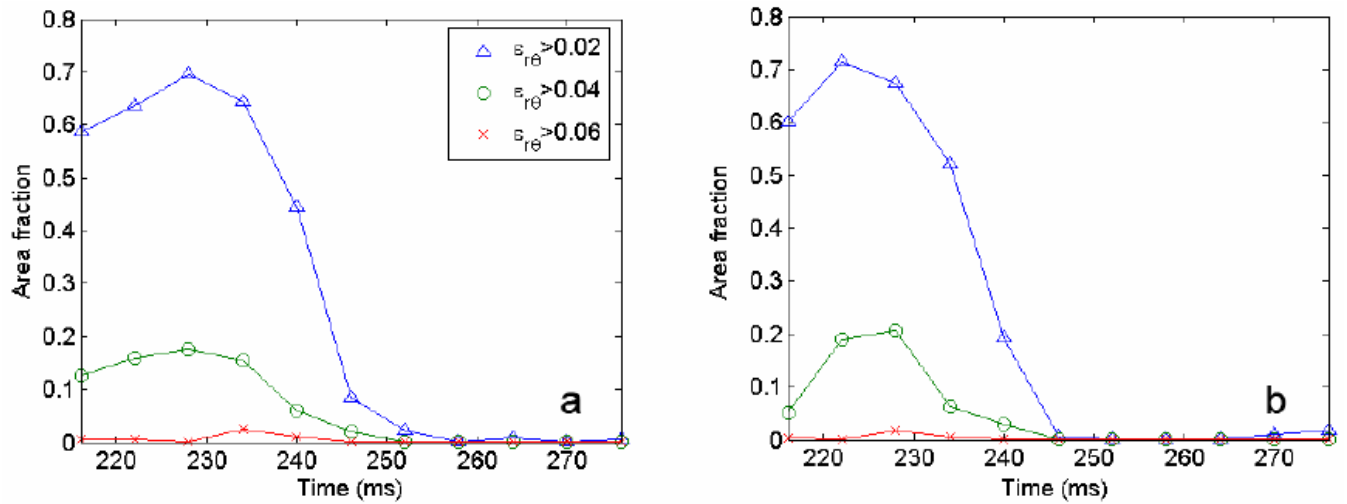
Figure 12.
Fraction of image area in which radial-circumferential shear strain $\varepsilon_{r\theta}$ exceeds a specified threshold, ε. Data are from the strain fields shown in Figure 9 (axial plane +2 cm above the reference plane), plotted vs. time after impact. (a) Subject S1. (b) Subject S2.
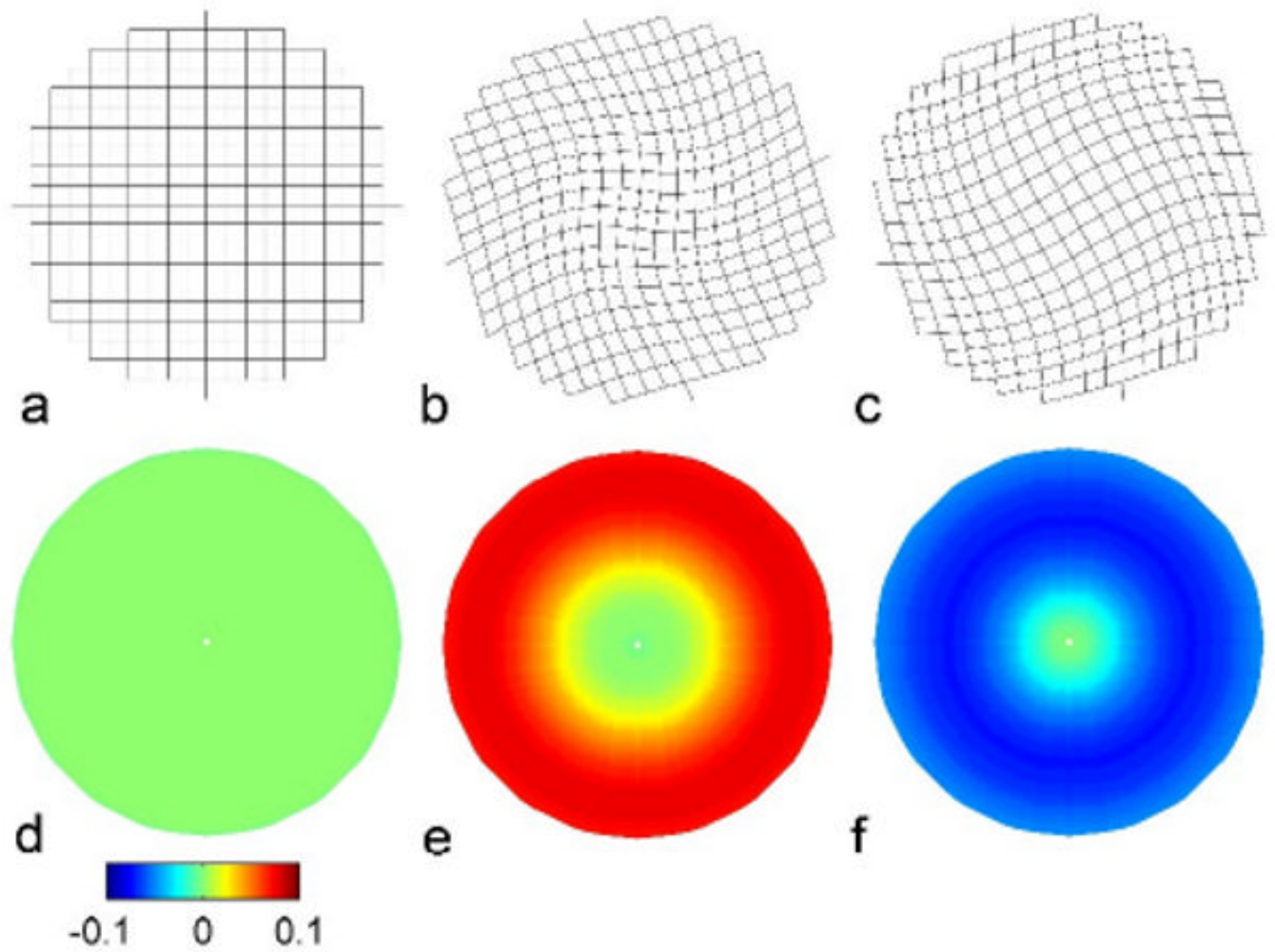
Figure 13.
Analytical predictions of shear deformation in a homogeneous, viscoelastic gel cylinder (instantaneous shear modulus G_0 = 1710 Pa; long term shear modulus G_∞ =1334 Pa; time constant τ = 1.3 ms) contained in a rigid shell subjected to angular acceleration half-sine pulse of 40 ms duration and 250 rad/s^2 amplitude. (a-c) Deformation of "tag" lines at t=0 and times of maximal and minimal shear deformation. (d-f) Corresponding radial-circumferential shear strains $\varepsilon_{r\theta}$.